Sensorless External Force Separation Method for Pedestrian Force Manipulation in Low-Speed Unmanned Electric Vehicles

Hongyuan Xing, Binh-Minh Nguyen, Osamu Shimizu, Hiroshi Fujimoto
The University of Tokyo
5-1-5, Kashiwanoha, Kashiwa, Chiba, 277-8561, Japan
xing.hongyuan24@edu.k.u-tokyo.ac.jp
nguyen.binhminh@edu.k.u-tokyo.ac.jp, shimizu.osamu@edu.k.u-tokyo.ac.jp, fujimoto@k.u-tokyo.ac.jp

***Abstract*—This paper proposes a method for sensorless separation of external forces acting on low-speed unmanned electric vehicles (EVs) to address a weakness in pedestrian force manipulation, specifically the issue of EVs stopping upon contact with road surface irregularities. This study focuses on suspension resonance transmitted to the wheels, which occurs only during contact with road surface irregularities. In the proposed method, the suspension resonance frequency components of the external forces acting on the wheels are estimated in real time, and their magnitudes are evaluated to achieve external force separation. Experiments were conducted using two types of bumps and two people to confirm that the proposed method enables a low-speed unmanned EV to separate the forces exerted by pedestrians and road surface irregularities, and to stop only when a pedestrian touches the vehicle.**

***Index Terms*—Electric Vehicle, Pedestrian Force Manipulation, External Force Separation, Sensorless Force Control, Backdrivability, Impedance Control, Disturbance Observer**

I. Introduction

In recent years, technologies such as unmanned parking at low-speeds and automatic summoning to the owner in parking lots have been developed, and due to their convenience, these technologies have been widely accepted in society [1], [2]. However, external sensors installed in autonomous vehicles, such as RGB cameras, millimeter-wave radars, and LiDARs, are sensitive to external factors. Particularly in crowded environments such as parking lots, where pedestrians and vehicles are in close proximity, there is room for improvement in accurately detecting the distance to pedestrians [3].

Our research group has devised a control method using an In-wheel Motor Electric Vehicle (IWM-EV), which integrates drive motors into the wheels. This technology enables the vehicle to stop smoothly when lightly touched by a pedestrian during low-speed operation, as shown in Fig. 1, without using external sensors. Additionally, when the pedestrian releases the EV, the vehicle resumes moving, creating a human interface that makes the EV feel light. This method is particularly applicable in scenarios such as low-speed of around 1 - 2 $\mathrm{m/s}$ autonomous parking and automatic summoning in parking lots where vehicles and pedestrians are in close proximity, and it enables mutual complementarity with external sensors [4]. Our research group refers to this technology as "Pedestrian Force Manipulation (PFM)", which utilizes the high responsiveness and robot-like independent drive characteristics of IWM-EVs [4]–[6], and employs sensorless impedance control often used in collaborative robots, enabling the manipulation of large-mass systems such as EVs with minimal force [7]–[9]. The force exerted by the pedestrian is estimated using a disturbance observer (DOB) without the use of force sensors [10], [11].

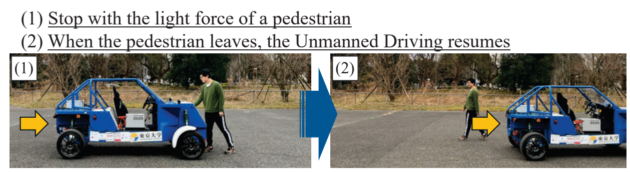

Fig. 1: Problem setting in PFM.

Since PFM does not rely on external sensors, it resolves the pedestrian detection issues of external sensors at close range. However, this control method has a critical drawback: impedance control is applied to all external forces acting on the vehicle. As a result, external forces from road surface irregularities are inevitably misinterpreted as forces from pedestrians, causing the vehicle to stop when encountering bumps or displacements on the road. While this method is primarily intended for use in parking lots, the presence of numerous road surface irregularities, such as wheel-locking plates and speed bumps, reduces its practicality.

This paper proposes a model and a control method to enable sensorless separation of external forces caused by road surface irregularities and those caused by pedestrians, which is verified through simulations and experiments. With the proposed method, the practicality of PFM is enhanced, and the vehicle can smoothly stop when pushed by a pedestrian while passing through road surface irregularities

II. Problem formulation

A. Experimental Equipment

Fig. 2 shows the experimental vehicle, FPEV5, owned by our laboratory. This vehicle is equipped with an in-wheel motor (IWM) on the left rear wheel and an ADSP-ACEDS1007

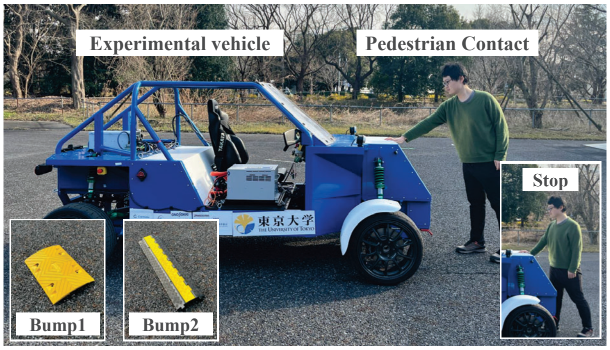

Fig. 2: Experimental vehicleFPEV-5. The Bump1 is round with the width of 50 cm, the depth of 35 cm, and the height of 4.5 cm. The Bump2 is trapezoidal inshape with the topbase of 18 cm, the bottom of 30 cm, and the height of 5.3 cm .

TABLE I: Vehicle Parameters

Symbol	Value	Symbol	Value
M	1094 kg	k_s	40 000 N/m
m_1	80 kg	c_s	1600 N/(m s)
J_ω	1.24 kg m^2	k_t	470 000 N/m
r	0.294 m	c_t	1370 N/(m s)
l_f, l_r	1.44 m, 1.11 m	θ_{gr}	0.222 rad

processor board. Wheel speed is measured using an encoder with a 14-bit resolution. The suspension adopts a double-wishbone system, with an instantaneous center of rotation (ICR) present only on the rear wheels. The vehicle parameters are summarized in Table I, and the meanings of each parameter are explained in section III.

In the experiments, as shown in Fig. 2, two types of road surface irregularities were used: Bump1, which is typically used in parking lots, and Bump2, which simulates a closed wheel-locking plate. As shown in Fig. 2, in the pedestrian-EV contact scenario, the pedestrian extends their arm to make contact with the moving EV, and as the arm bends, the EV comes to a smooth stop.

B. Pedestrian Force Manipulation

The block diagram of the PFM is shown in Fig. 3 [4]. The previous research is composed of three algorithms:

1) **Speed Control**
When no external force is applied to the vehicle body, speed control is executed, and the vehicle travels at a constant speed. where the speed reference is V_o and the proportional control is used for the speed controller.
2) **External Force Estimation via a Disturbance Observer**
DOB is used to estimate the external force F_{ext} applied by the pedestrian to the EV. P_n^{-1} represents the inverse model of the nominal plant model, Q is a low-pass filter, and F_d is the compensatory value for running resistance determined. The transfer function from input torque T to output vehicle speed V, which is assumed to be identical to the wheel speed, is represented as follows based on equations of motion:

$$P_n = \frac{V}{T} = \frac{r}{(4J_\omega + r^2 M)s}, \tag{1}$$

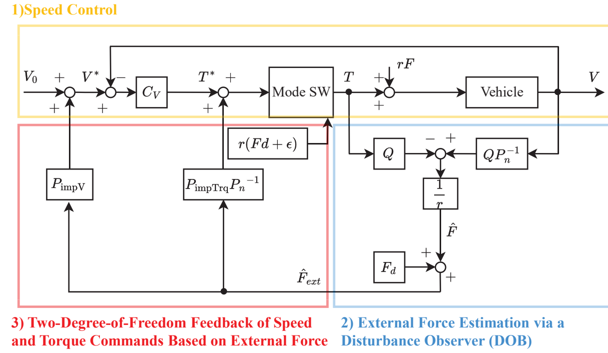

Fig. 3: Block diagram of the conventional method.

where r is the wheel radius, J_ω is the wheel inertia, and M is the vehicle masses.
3) **Two-Degree-of-Freedom Feedback of Speed and Torque Commands Based on External Force**
This method uses impedance control with a two-degree-of-freedom feedback system, where virtual mass and viscosity are applied to the estimated external force $\hat{F}_{ext}$, which is calculated as $\hat{F}_{ext} = \hat{F} - F_d$. Based on this control system, the speed command and torque command values decrease smoothly in response to the external force, only while the external force is applied to the EV. Here, since the elasticity and viscosity of the pedestrian's arm are variable, any error between $\hat{F}_{ext}$ and the actual force is still covered, even if such an error occurs. The nominal model for the impedance control is defined as, $P_{imp\mathrm{V}} = \frac{1}{m_\mathrm{V}s+b_\mathrm{V}}$ and $P_{imp\mathrm{Trq}} = \frac{1}{m_\mathrm{T}s+b_\mathrm{T}}$, where m_V and b_V are the virtual mass and virtual viscosity for speed feedback, and m_T and b_T are the virtual mass and virtual viscosity for torque feedback, respectively.
At very low speeds, a constant torque $T = r(F_d + \epsilon)$ is output. Pedestrians can stop the vehicle by applying a force that balances ϵ. When the pedestrian releases their hand, the vehicle accelerates, and the system returns to speed control mode.

Here, a drawback of PFM is that during contact with road surface irregularities, the reaction forces acting on the vehicle are also fed back, causing the vehicle to stop.

III. Sensorless External Force Separation Method Focusing on Sprung Resonance Frequency

A. System Modeling

This subsection describes a model of the rear-wheel drive IWM-EV. In this paper, only straight-line driving is considered, and a model is used in which the front and rear wheels are connected to the vehicle body via suspension, as shown in Fig. 4. Assuming that the front and rear wheels move integrally with the vehicle body during the longitudinal motion of the vehicle, the motion equation of the vehicle body is expressed as follows:

$$M\dot{V} = 2\sum_{j=f,r} F_{x,j} - F_{\mathrm{body}} - F_{air}, \tag{2}$$

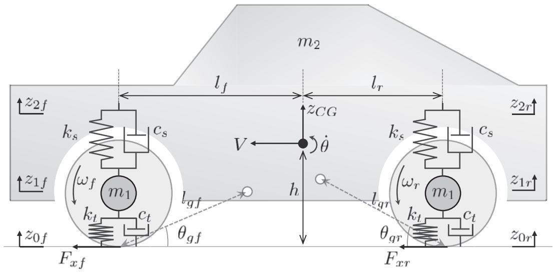

Fig. 4: Vehicle motion model.

where $F_{x,j}$ is the driving force of the front or rear wheels, F_{air} is the air resistance, and F_{body} is the external force applied to the vehicle body. The subscript j represents f (front) or r (rear) (this notation will be followed hereafter).

The wheel rotational motions are expressed as follows:

$$J_\omega \dot{\omega}_j = T_j - rF_{x,j} - rF_{\text{wheel},j} - rC_\omega F_{z,j} - M_{\text{sus},j}, \quad (3)$$

where ω_j is the angular velocity of the wheels, T_j is the motor torque of the wheels, and $T_r = T$, $T_f = 0$. $F_{\text{wheel},j}$ is the external force in the rotational direction of the wheels, C_ω is the rolling resistance coefficient, $F_{z,j}$ is the vertical load on the wheels, and $M_{\text{sus},j}$ is the torque disturbance from the suspension force.

The relationship between the vehicle speed V and the wheel speed ω_j of the wheels is expressed as follows:

$$V = r\omega_j \quad (4)$$

The pitch motion and vertical motion of the vehicle body are expressed as follows:

$$I_y \ddot{\theta} = -l_f(F_{sf} + F_{gzf}) + l_r(F_{sr} + F_{gzr}), \quad (5)$$
$$m_2 \ddot{z}_{CG} = F_{sf} + F_{gzf} + F_{sr} + F_{gzr} - m_2 g, \quad (6)$$
$$m_{2,j} \ddot{z}_{2,j} = F_{s,j} + F_{gz,j} - m_{2,j} g, \quad (7)$$

where F_{sf} and F_{sr} are the front and rear suspension forces, F_{gzf} and F_{gzr} are vertical forces from suspension geometry, g is gravitational acceleration, θ is the pitch angle, I_y is pitch inertia, l_f and l_r are distances from the axles to the COG, z_{CG} is the COG's vertical displacement, m_2 is half the vehicle body mass, $m_{2,j}$ is front - rear distribution of m_2 ($2m_{2,j} \simeq m_2$) and $z_{2,j}$ is the vertical displacement of the body above the wheels ($z_{2f} = z_{CG} - l_f\theta$, $z_{2r} = z_{CG} + l_r\theta$).

The vertical motion of the front and rear wheels are expressed as follows:

$$m_1 \ddot{z}_{1,j} = -F_{s,j} - F_{gz,j} + F_{z,j} - m_{1,j} g, \quad (8)$$
$$F_{s,j} = -k_s(z_{2,j} - z_{1,j}) - c_s(\dot{z}_{2,j} - \dot{z}_{1,j}) + F_{s,j0}, \quad (9)$$
$$F_{z,j} = -k_t(z_{1,j} - z_{0,j}) - c_t(\dot{z}_{1,j} - \dot{z}_{0,j}) + F_{z,j0} \quad (10)$$

where $z_{1,j}$ is the distance from the center of the wheels to the ground. The parameters k_s and c_s denote the spring stiffness and damping coefficient of the suspension, respectively, while $z_{0,j}$ is the displacement of the contact point of the wheels. k_t and c_t represent the tire stiffness and damping coefficients, respectively. Lastly, $F_{s,j0}$ and $F_{z,j0}$ are constants representing the static suspension force and static vertical load for the wheels.

The inclination angles θ_{gf} and θ_{gr} from the contact points of the front and rear wheels to the suspension rotation center are the ICR inclination angles of the front and rear wheels, respectively. When the suspension force $F_{s,j}$ is generated as the wheels contact road surface irregularities, a moment $M_{\text{sus},j}$ is generated around the ICR and transmitted to the wheels as a torque disturbance, as expressed in [12].

$$M_{\text{sus}f} = -(F_{sf} - F_{sf0}) \cdot l_{gf} \cos\theta_{gf}, \quad (11)$$
$$M_{\text{sus}r} = (F_{sr} - F_{sr0}) \cdot l_{gr} \cos\theta_{gr} \quad (12)$$

B. Fundamental idea of force separation

When a pedestrian comes into contact with a moving vehicle, an external force is applied in the traveling direction of the vehicle body, and the estimated external force from drive wheel DOB $\hat{F} = \hat{F}_{\text{human}}$ is expressed as follows:

$$\hat{F}_{\text{human}} \simeq -F_{\text{body}} - F_{\text{air}} - 2\sum_{j=f,r} C_\omega F_{z,j0} \quad (13)$$

When a vehicle contacts road irregularities, an external force is applied in the wheel's rotational direction, and a change occurs at the wheel contact point, z_{0f} or z_{0r}. From equations (10), (11), (12), and (3), the vertical external force $M_{\text{sus},j}/r$ and F_{zr} propagate to the wheel's external force. Since the experimental vehicle has an instantaneous center of rotation (ICR) only at the rear wheels, $M_{\text{sus}f} = 0$, and $M_{\text{sus}r} + rC_\omega F_{zr} \gg rC_\omega(F_{zf} - F_{zf0})$. The vertical external force $M_{\text{sus}r}/r + C_\omega F_{zr}$ is defined as F_v, and the external force estimated by the disturbance observer (DOB) from the driving wheel, $\hat{F} = \hat{F}_{\text{road}}$, is expressed as follows:

$$\hat{F}_{\text{road}} \simeq -2\sum_{j=f,r} F_{\text{wheel},j} - F_{\text{air}} - 2C_\omega F_{zf0} - 2F_v \quad (14)$$

Here, the transfer function from z_{0r} to $M_{\text{sus}r}$ is given by:

$$\frac{M_{\text{sus}r}(s)}{z_{0r}(s)} = V_{Mz}(s) = \frac{n_{v4}s^4 + n_{v3}s^3 + n_{v2}s^2}{d_{v4}s^4 + d_{v3}s^3 + d_{v2}s^2 + d_{v1}s^1 + d_{v0}}, \quad (15)$$

where $n_{v4} = ac_sc_t, n_{v3} = a(c_sk_t + c_tk_s), n_{v2} = ak_sk_t, d_{v4} = m_2m_1, d_{v3} = m_2c_t + m_2c_s + 2m_1c_s, d_{v2} = m_2k_s + m_2k_t + 2m_1k_s + 2c_sc_t, d_{v1} = 2c_sk_t + 2c_tk_s, d_{v0} = 2k_sk_t, a = m_2l_{gr}\cos\theta_{gr}$. Here, since it is generally the case that $k_t \gg k_s \gg c_s$, the relationships $d_{v2} \simeq m_2k_s + m_2k_t + 2m_1k_s + 2c_s^2 + 2c_sc_t$, $d_{v1} \simeq 4c_sk_s + 2c_sk_t + 2c_tk_s$, and $d_{v0} \simeq 2k_s^2 + 2k_sk_t$ are established, leading to the following approximation:

$$V_{Mz}(s) \simeq V_{z_{21}}(s) \cdot V_{z_{10}|z_2:0}(s) \cdot l_{gr}\cos\theta_{gr} m_2 s^2, \quad (16)$$

$V_{z_{21}}(s)$ and $V_{z_{10}|z_2:0}(s)$ are the transfer functions from $z_{1,j}$ to $z_{2,j}$ derived from equations (7) and (9), and from $z_{0,j}$ to $z_{1,j}$ derived from equations (8), (9), and (10) with $z_{2,j} = 0$, respectively, and are expressed as follows:

$$V_{z_{21}}(s) = \frac{c_s s + k_s}{m_2 s^2 + 2c_s s + 2k_s}, \quad (17)$$

$$V_{z_{10}|z_2:0}(s) = \frac{c_t s + k_t}{m_1 s^2 + (c_s + c_t)s + k_s + k_t} \quad (18)$$

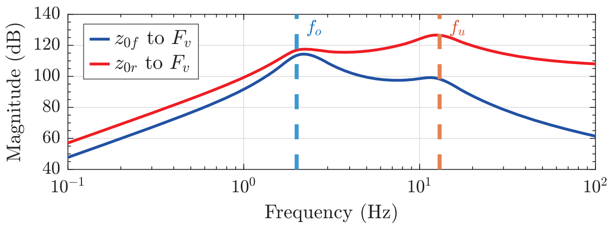

Fig. 5: The frequency response from z_{0f} and z_{0r} to F_v

Similarly, the transfer function from z_{0r} to F_{zr} is given by:

$$\frac{F_{zr}(s)}{z_{0r}(s)} = V_{Mz}(s) \cdot \frac{m_2 m_1 s^2 + (m_2 + 2m_1)(c_s s + k_s)}{l_{gr} \cos\theta_{gr} m_2 \cdot (c_s s + k_s)}, \tag{19}$$

Defining equation (19) as $V_{Mz}(s) \cdot G_{F_z M}(s)$, the transfer function from z_{0r} to F_v is given as follows:

$$\frac{F_v(s)}{z_{0r}(s)} = V_{Mz}(s) \cdot \left(C_\omega G_{F_z M}(s) + 1/r\right), \tag{20}$$

Since $V_{Mz}(s)$ includes the product of the two second-order systems $V_{z_{21}}(s)$ and $V_{z_{10}|z_2:0}(s)$, F_v resonate at the following frequencies as z_{0r} changes:

$$f_o = \frac{1}{2\pi}\sqrt{\frac{2k_s}{m_2}}, \quad f_u = \frac{1}{2\pi}\sqrt{\frac{k_s + k_t}{m_1}}, \tag{21}$$

where f_o and f_u are referred to as the sprung mass resonance frequency and the unsprung mass resonance frequency, respectively, which are inherent vibrations determined solely by the vehicle parameters. The resonance frequencies of the experimental vehicle can be approximated as $f_o \simeq 2\,\mathrm{Hz}$ and $f_u \simeq 12\,\mathrm{Hz}$ using the parameters in Table I.

The transfer functions from z_{0f} to F_v are given by:

$$\frac{F_v(s)}{z_{0f}(s)} = G_{F_{rf}}(s) \cdot V_{Mz}(s) \cdot \left(C_\omega G_{F_z M}(s) + 1/r\right), \tag{22}$$

$G_{F_{rf}}(s)$ is the transfer function from F_{sf} to F_{sr} and is expressed as follows:

$$G_{F_{rf}}(s) = \frac{n_{g3}s^3 + n_{g2}s^2 + n_{g1}s^1 + n_{g0}}{d_{g4}s^4 + d_{g3}s^3 + d_{g2}s^2 + d_{g1}s^1 + d_{g0}}, \tag{23}$$

where $n_{g3} = bm_1c_s, n_{g2} = b(m_1k_s + c_s^2 + c_sc_t), n_{g1} = b(2c_sk_s - c_s + c_sk_t + c_tk_s), n_{g0} = b(k_s^2 - k_s + k_sk_t), d_{g4} = I_y m_2 m_1, d_{g3} = I_y m_2(c_s + c_t) + cn_{g3}, d_{g2} = I_y m_2(k_s + k_t) + cn_{g2}, d_{g1} = cn_{g1}, d_{g0} = cn_{g0}, b = m_2 l_f l_r - I_y, c = (m_2 l_r^2 + I_y)/b$.

Fig.5 shows the frequency response from z_{0f} and z_{0r} to F_v based on equations (20), (22), and Table 1. During z_{0r} fluctuations, F_v exhibits resonance components near f_o and f_u. On the other hand, during z_{0f} fluctuations, the resonance component near f_o remains nearly unchanged, while the resonance component near f_u is attenuated.

Based on the above observations and equations (13) and (14), it can be concluded that the estimated external force $\hat{F}$ acting on the drive wheels contains the external force F_v with resonance components at f_o and f_u only when the front or rear wheels of the vehicle are in contact with road surface irregularities, causing changes in z_{0f} and z_{0r}.

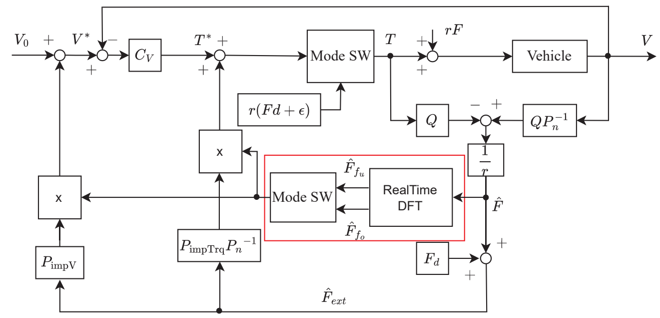

Fig. 6: Block diagram of the proposed method.

C. Method for External Force Separation

TABLE II: Mode Switch Algorithm.

State	Discrimination	Control
$\hat{F}_{f_o} > \alpha$ or $\hat{F}_{f_u} > \beta$	Road Surface Irregularities	Speed Control
Other	Pedestrian	PFM

The block diagram of the proposed method is shown in Fig. 6, where the red frame highlights the external force classification part. As described in the previous section, the estimated external force $\hat{F}$ on the drive wheels contains F_v components at f_o and f_u only during contact with road surface irregularities. Therefore, a Discrete Fourier Transformation (DFT) is performed on $\hat{F}$ to extract the f_o and f_u components, $\hat{F}_{f_o}$ and $\hat{F}_{f_u}$, in real-time. Based on their magnitudes, the external force is separated without using sensors.

From Table II, when an external force is applied and $\hat{F}_{f_o}$ or $\hat{F}_{f_u}$ exceeds thresholds α or β, the vehicle moves at a constant speed over road irregularities; otherwise, PFM is performed. The thresholds are determined experimentally, accounting for slight vibrations due to pitching during pedestrian contact.

Through this control method, the low-speed unmanned EV can pass over road surface irregularities and stop with light force only during pedestrian contact.

The real-time DFT is performed using the Goertzel algorithm. The Goertzel algorithm uses a recursive filter to extract only specific frequency components, making it faster than the Fast Fourier Transform (FFT) and more suitable for real-time analysis [13].The Goertzel algorithm equations are as follows:

$$s[n] = x[n] + 2\cos\left(\frac{2\pi q}{N}\right)s[n-1] - s[n-2] \tag{24}$$

$$X_q = s[N-1] - e^{-\frac{2\pi i q}{N}} s[N-2] \tag{25}$$

Here, $s[n]$ is the state variable at the nth sample, F_s is the sampling frequency, $q = f \cdot N/F_s$ is the tuning value corresponding to the target frequency f, N is the data length, and X_q represents the resulting frequency component.

IV. Evaluation of External Force Separation

In this section, simulations and experiments are conducted to validate the external force separation model presented in

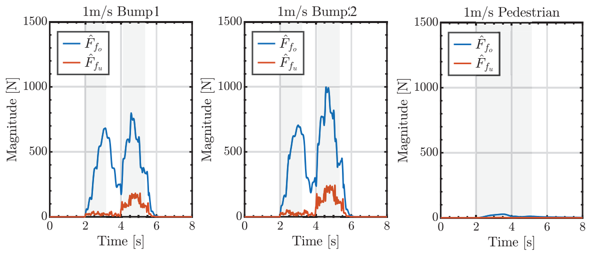

Fig. 7: Simulation results of $\hat{F}_{f_o}$ and $\hat{F}_{f_u}$ when contacting and passing over a bump or pedestrian at a constant speed.

Section III. The analysis focuses on the f_o component $\hat{F}_{f_o}$ and the f_u component $\hat{F}_{f_u}$ of the estimated external force acting on the rear wheels, $\hat{F}$, when an EV comes into contact with and passes over a bump or a person at a constant speed.

For the extraction of $\hat{F}_{f_o}$ and $\hat{F}_{f_u}$, an offline estimation of the rear wheel external force $\hat{F}$ is performed, followed by the application of FFT using a window function with 1000 samples per second, updated every $1\,\mathrm{ms}$. To account for variations in f_o and f_u caused by parameter fluctuations due to occupant weight, tire pressure, and quantization errors, the maximum values of $f_o \pm 1\,\mathrm{Hz}$ and $f_u \pm 1\,\mathrm{Hz}$ are defined as $\hat{F}_{f_o}$ and $\hat{F}_{f_u}$, respectively.

A. Simulation Results

In the simulations, the vehicle model presented in Section III and the vehicle parameters listed in Table 1 were utilized. The simulations were conducted using MATLAB/Simulink. A constant speed control with a velocity command of $1\,\mathrm{m/s}$ was performed. The bump model was based on a model resembling Bump1 and Bump2, as shown in Fig. 2, and the pedestrian model employed a spring-damper system simulating human antagonistic muscles. The spring coefficient was set to $k_h = 100$ and the damping coefficient to $c_h = 20$, following previous research [4].

Fig. 7 illustrate $\hat{F}_{f_o}$ and $\hat{F}_{f_u}$ during the periods when the vehicle contacts and passes over a bump and when it contacts and passes over a pedestrian, respectively, with the gray areas representing the contact periods. During the front wheel passage over the bump, only $\hat{F}_{f_o}$ increases, while during the rear wheel passage, both $\hat{F}_{f_o}$ and $\hat{F}_{f_u}$ increase. No noticeable increase is observed during pedestrian contact. Therefore, these results align with the model proposed in Section III.

Additionally, during the simulation, both the FFT and the Goertzel algorithm were applied online to $\hat{F}$, and the computation time for each method was measured. As a result, the Goertzel algorithm achieved a $41.7\,\%$ reduction in computation time compared to the FFT.

B. Experimental Results

The first row of Fig. 8 shows the experimental results of $\hat{F}_{f_o}$ and $\hat{F}_{f_u}$ when the EV contacts and passes over the two types of bumps and a pedestrian, with a constant speed control of $1\,\mathrm{m/s}$ as shown in Fig. 2. The second row shows the experimental results for the case of $2\,\mathrm{m/s}$. The pedestrian applied force in front of the vehicle for approximately $3\,\mathrm{s}$ during constant speed driving, and then moved away from the vehicle.

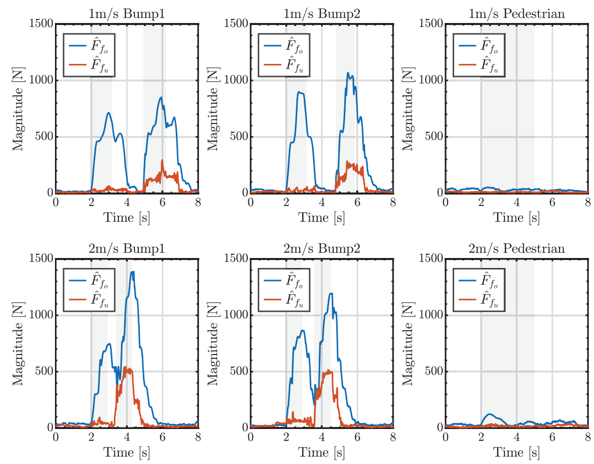

Fig. 8: Experimental results of $\hat{F}_{f_o}$ and $\hat{F}_{f_u}$ when contacting and passing over a bump or pedestrian at a constant speed.

By focusing on Fig. 8, it can be observed that, regardless of the vehicle speed or the bump shape, $\hat{F}_{f_o}$ and $\hat{F}_{f_u}$ only increase during the periods when the front or rear wheels of the vehicle pass over the bumps.

The experimental results confirm that f_o and f_u do not change with the vehicle's speed or the road surface displacement shape, as indicated by equations (20), thereby proving the correctness of the proposed model.

V. Validation of the Proposed Method

In this section, the effectiveness of the proposed method was experimentally validated using two types of bumps and two pedestrians with a weight difference of approximately $30\,\mathrm{kg}$, as shown in Fig. 2. The experimental setup is illustrated in Fig. 9, where the bump contact point was positioned approximately $7.5\,\mathrm{m}$ from the control start point, and the pedestrian contact point was set at approximately $15\,\mathrm{m}$. In the experiment, the parameters were set as $m_\mathrm{V} = 170$, $m_\mathrm{T} = 550$, $b_\mathrm{V} = 140$, and $b_\mathrm{T} = 120$. The pole of the P-control was set to 0.6, and the pre-contact velocity command V_o was set to $1\,\mathrm{m/s}$. Additionally, the control switching thresholds α and β were determined based on the magnitudes of $\hat{F}_{fo}$ and $\hat{F}_{fu}$ during 10 trials where pedestrians stopped the EV, resulting in $\alpha = 85$ and $\beta = 50$. The extraction of $\hat{F}_{f_o}$ and $\hat{F}_{f_u}$ employed the same method as described in Section IV, using the real-time Goertzel algorithm.

Fig. 10, Fig. 11, and Fig. 12 illustrate the wheel velocity V, the velocity command V^*, and the vehicle position X (integrated value of V) for both the conventional methods $(V_\mathrm{conv}, V^*_\mathrm{conv}, X_\mathrm{conv})$ and proposed methods $(V_\mathrm{prop}, V^*_\mathrm{prop}, X_\mathrm{prop})$ under different scenarios involving bumps and pedestrians. Additionally, the vertical dashed lines in Fig. 10 and Fig. 11 indicate the time of bump contact, while the gray areas represent the duration during which the pedestrian is in contact with the EV in the proposed method. In Fig. 12, the gray

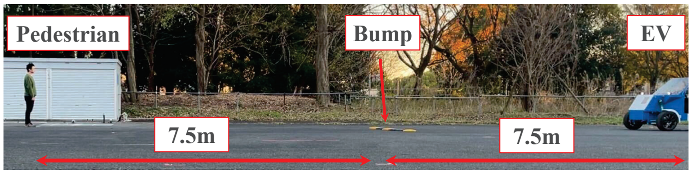

Fig. 9: Experimental Setup.

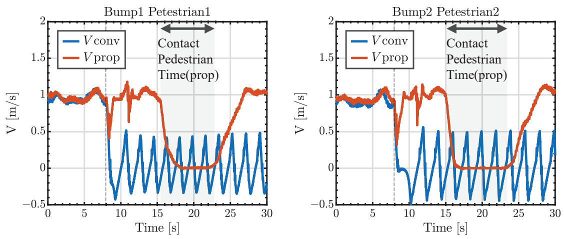

Fig. 10: Experimental results of the wheel velocity V of EV.

areas indicate the positions of the bump and the pedestrian, respectively.

From the experimental results, it can be observed that under both conditions, when using the conventional method, V^* becomes negative upon bump contact, and the vehicle cannot proceed further. In contrast, with the proposed method, sensorless external force separation is performed, and V^* remains at $1\,\mathrm{m/s}$ during bump contact. The velocity command V^* decreases only during pedestrian contact, and once the pedestrian releases their hand, the vehicle resumes motion.

Additionally, from Fig. 12, it can be confirmed that regardless of the bump or pedestrian condition, while the conventional method causes the EV to stop upon bump contact, the proposed method allows the vehicle to pass over the bump and stop only while the pedestrian is in contact with the vehicle.

VI. Conclusion

The study addressed the issue of EVs stopping when encountering road surface displacements, as part of realizing Pedestrian Force Manipulation for Low-Speed Unmanned EVs. A sensorless external force separation method was proposed, focusing on the spring resonance frequency caused by the external forces on the driving wheels during contact with road surface displacements.

The proposed model was analyzed through simulation and experiment. Additionally, experiments were conducted with two pedestrians and two types of bumps to compare the conventional method and the proposed method, verifying the effectiveness of the proposed approach.

Future plans include comparisons with sensors, separation of external forces from road inclinations, integration with IoT systems, and coordination with path planning.

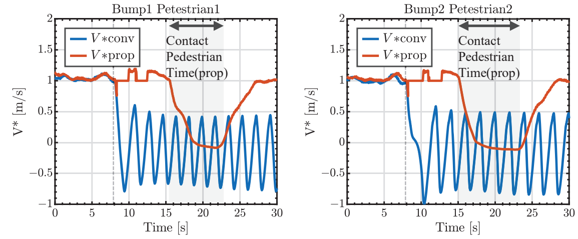

Fig. 11: Experimental results of the velocity command V^* of EV.

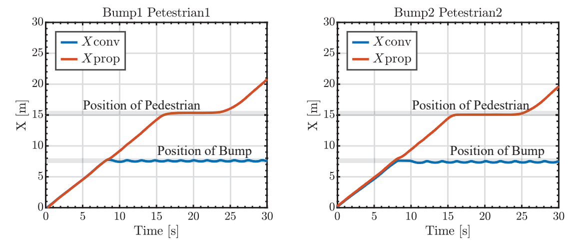

Fig. 12: Experimental results of the position X of EV.

References

[1] X. Zhang, X. Xia, S. Liu, Y. Cao, J. Li, and W. Guo, "An integrated framework on autonomous-ev charging and autonomous valet parking (avp) management system," *IEEE Transactions on Transportation Electrification*, vol. 8, no. 2, pp. 2836–2852, 2022.

[2] Y. Zhong, W. Wen, and L.-T. Hsu, "Towards accurate vehicle-to-pedestrian relative positioning aided by inter-frame and inter-agent gnss measurement collaboration using factor graph optimization for smart summon," in *he 36th International Technical Meeting of the Satellite Division of The Institute of Navigation (ION GNSS+ 2023)*, pp. 3104–3116, 2023.

[3] T. Verstraete and N. Muhammad, "Pedestrian collision avoidance in autonomous vehicles: A review," *Computers*, vol. 13, no. 3, 2024.

[4] K. Yonezawa and H. Fujimoto, "Human-vehicle-interaction system with unmanned driving ev in parking lots by impedance control," in *The IEEJ International Workshop on Sensing, Actuation, Motion, Control, and Optimization*, 2022.

[5] T. Emmei and H. Fujimoto, "Force control of in-wheel-motored electric vehicles," *IEEJ Journal of Industry Applications*, vol. 9, no. 4, pp. 384–391, 2020.

[6] L. Hott, V. Ivanov, K. Augsburg, V. Ricciardi, M. Dhaens, M. A. Sakka, K. Praet, and J. V. Molina, "Ride blending control for awd electric vehicle with in-wheel motors and electromagnetic suspension," in *2020 IEEE Vehicle Power and Propulsion Conference (VPPC)*, pp. 1–5, 2020.

[7] T. Murakami, R. Nakamura, F. Yu, and K. Ohnishi, "Force sensorless impedance control by disturbance observer," in *Conference Record of the Power Conversion Conference - Yokohama 1993*, pp. 352–357, 1993.

[8] S. U. Chowarit Mitsantisuk, Kiyoshi Ohishi and S. Katsura, "Kalman filter-based disturbance observer and its applications to sensorless force control," *Advanced Robotics*, vol. 25, no. 3-4, pp. 335–353, 2011.

[9] G. M. Razvan Andrei Budau Petrea, Roberto Oboe, "Safe high stiffness impedance control for series elastic actuators using collocated position feedback," *IEEJ Journal of Industry Applications*, vol. 12, no. 4, pp. 735–744, 2023.

[10] E. Sariyildiz, R. Oboe, and K. Ohnishi, "Disturbance observer-based robust control and its applications: 35th anniversary overview," *IEEE Transactions on Industrial Electronics*, vol. 67, no. 3, pp. 2042–2053, 2020.

[11] K. Shimamoto and T. Murakami, "Force sensorless hybrid position/force control with equivalent mass matrices switching for decoupled rubbing motion," *IEEJ Journal of Industry Applications*, vol. 12, no. 2, pp. 107–116, 2023.

[12] H. Ichikawa, T. Ueno, O. Shimizu, and H. Fujimoto, "Model building and experimental validation for regeneration of perpendicular vibration by in-wheel motor," in *2024 IEEE International Conference on Advanced Intelligent Mechatronics (AIM)*, pp. 1213–1218, 2024.

[13] R. Lora-Rivera, O. Oballe-Peinado, A. Trujillo-Leon, and F. Vidal-Verdu, "The goertzel algorithm for the extraction of texture features," *IEEE Robotics and Automation Letters*, vol. 9, no. 8, pp. 6928–6934, 2024.